LETTER • **OPEN ACCESS**

Fractional quantum Hall effect in CVD-grown graphene

To cite this article: M Schmitz *et al* 2020 *2D Mater.* **7** 041007

IOP Publishing 2D Mater. 7 (2020) 041007 https://doi.org/10.1088/2053-1583/abae7b

2D Materials

OPEN ACCESS

RECEIVED
19 May 2020

REVISED
3 August 2020

ACCEPTED FOR PUBLICATION
12 August 2020

PUBLISHED
10 September 2020

LETTER

Fractional quantum Hall effect in CVD-grown graphene

M Schmitz[1,2], T Ouaj[1,2], Z Winter[1,2], K Rubi[3], K Watanabe[4], T Taniguchi[5], U Zeitler[3], B Beschoten[1] and C Stampfer[1,2]

[1] JARA-FIT and 2nd Institute of Physics, RWTH Aachen University, 52074 Aachen, Germany, EU
[2] Peter Grünberg Institute (PGI-9), Forschungszentrum Jülich, 52425 Jülich, Germany, EU
[3] High Field Magnet Laboratory (HFML-EMFL), Radboud University, 6525 ED Nijmegen, The Netherlands, EU
[4] Research Center for Functional Materials, National Institute for Materials Science, 1-1 Namiki Tsukuba, Ibaraki 305-0044, Japan
[5] International Center for Materials Nanoarchitectonics, National Institute for Materials Science, 1-1 Namiki Tsukuba, Ibaraki 305-0044, Japan

E-mail: stampfer@physik.rwth-aachen.de

Keywords: graphene, fractional quantum Hall effect, CVD, magneto-transport, electronic properties

Abstract

We show the emergence of fractional quantum Hall states in graphene grown by chemical vapor deposition (CVD) for magnetic fields from below 3 T to 35 T where the CVD-graphene was dry-transferred. Effective composite-fermion filling factors up to $\nu^* = 4$ are visible and higher order composite-fermion states (with four flux quanta attached) start to emerge at the highest fields. Our results show that the quantum mobility of CVD-grown graphene is comparable to that of exfoliated graphene and, more specifically, that the $p/3$ fractional quantum Hall states have energy gaps of up to 30 K, well comparable to those observed in other silicon-gated devices based on exfoliated graphene.

Recent progress in device fabrication of graphene-based heterostructures allows for the observation of an increasing number of composite-fermion (CF) states in graphene [1–5]. The emergence and the level of manifestation of these states can be regarded as an ultimate proof of device quality in terms of quantum mobility, homogeniety and low residual impurities. Until present, the observation of such interaction-driven many-body states has been limited to devices based on mechanically exfoliated graphene, whereas it has been the subject of discussion whether chemical vapor deposition (CVD) could yield graphene hosting CF states at all.

Dry-transferred CVD-grown graphene has already been demonstrated to be able to compete with the transport properties of highest-quality exfoliated devices with average carrier mobilities exceeding 100 000 cm^2 $(Vs)^{-1}$, mean free paths of up to 28 μm and well-developed integer quantum Hall states at moderate magnetic fields [6–9]. Since these devices are only limited in size by the two-dimensional (2D) materials used for the dry pick-up [10], as well as limitations of the copper growth substrates, they might open the door to large-area high-quality devices enabling even better understanding of the physics of correlated electron systems resulting in CF states in graphene. It is therefore of great importance to establish whether the already high carrier mobilities observed in CVD graphene [6, 7, 11] also translates into sufficiently low residual charge carrier fluctuations, high enough homogeneities and quantum mobilities allowing for the clear emergence of correlation-induced states.

Here we show how to fabricate and characterize dry-transferred CVD-grown graphene heterostructures that show fractional quantum Hall states comparable to exfoliated graphene devices. The activation gaps extracted from these experiments are in good agreement with reported values for silicon-gate based samples and promise even richer CF state spectra when using latest generation of graphitic gating technologies as well as macroscopic devices promised by a CVD graphene based technology [12].

Graphene was grown using low-pressure chemical vapor deposition on the inside of copper foil enclosures [11, 13–15]. The Cu foils were heated up to 1035 °C within 45 minutes and were further annealed at this temperature for another 15 minutes under a constant flow of 15 sccm H_2 gas. This was followed by a 3 hour growth step under a flow of a H_2/CH_4 mixture (45/5 sccm) at the very same temperature. Afterwards the oven was switched off and the lid of the furnace was opened up for a rapid cool-down

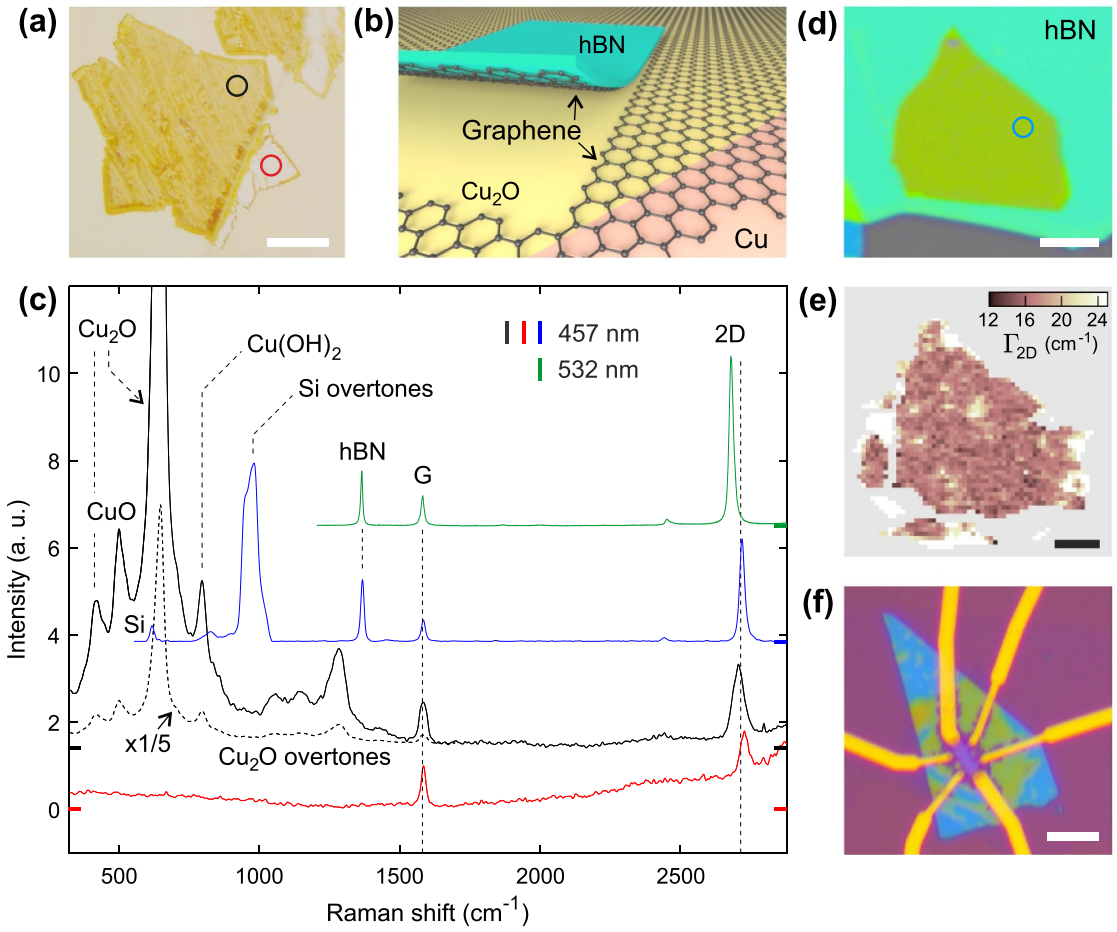

Figure 1. Device fabrication (a) Optical image of CVD-grown graphene (Gr) crystals on a Cu foil after a partially oxidized Cu/Gr interface. Scale bar is 25 μm. (b) Schematic illustration of the mechanical delamination process. (c) Raman spectra recorded with two different laser excitation wavelengths (457 nm and 532 nm, see color legend) at the locations highlighted by color matching circles (red and black) on the partially oxidized/non-oxidized copper/graphene areas shown in panel (a) and on the final hBN/CVD-Gr/hBN heterostructure in panel (d) (blue and green Raman spectra were measured at the circle). The spectra are shifted by constant offsets in intensity for comparability (see colored ticks on the right axis) and the black dashed spectrum is a scaled-down version of the black spectrum. (d) Optical image of a finished hBN/CVD-Gr/hBN heterostructure (scale bar is 5 μm). (e) Raman map showing the 2D line width Γ_{2D} of the graphene layer encapsulated in the heterostructure shown in panel (d) (scale bar is 5 μm). (f) Optical image of the etched and contacted hBN/CVD-Gr/hBN Hall bar structure (scale bar is 10 μm).

keeping the same gas mixture flow as before. This process yields large isolated single-layer graphene flakes with lateral sizes of several hundred micrometers, depending only on the growth time [6]. After growth, we stored the cut and unfolded Cu foils in a water-saturated air atmosphere (>99% relative humidity) at a temperature of 30 °C for two days (48 h). This accelerates the water-mediated oxidation process of the copper surface at the graphene/copper interface [16] and is of crucial importance to weaken the van der Waals adhesion forces between the graphene and the copper surface. The controlled oxidation process is therefore the key to a successful dry-transfer process, which is not possible with as-grown graphene on copper due to its strong bonding to the surface.

Figure 1(a) shows an optical image of a CVD-grown graphene crystal with a partially oxidized graphene/copper interface. The water intercalation and oxidation process can be monitored by confocal Raman spectroscopy when using a laser excitation wavelength of 457 nm (blue), see figure 1(c). We note that a Raman laser excitation wavelength of 532 nm (green) cannot be used to characterize graphene on copper as it creates a broad photoluminesence (PL) emission peak from the underlying Cu, which dominates the emission spectrum [17]. When using the shorter excitation wavelength, the PL emission from the Cu is shifted to larger wavenumbers thereby allowing to analyze all relevant Raman peaks up to 3000 cm^{-1}. Raman spectra recorded at the oxidized and non-oxidized areas (black and red spectra in figure 1(c), highlighted by color matching circles in figure 1(a)) show both the characteristic graphene Raman G and 2D peaks at $\omega_G = 1582$ cm^{-1} and

$\omega_{2D} = 2720\ \mathrm{cm}^{-1}$ [18]. The absence of the defect-related D peak around 1340 cm^{-1} in the spectra indicates that the graphene is grown defect-free [19] and remains virtually undamaged by the oxidation process. In further comparison of the two spectra, we denote the emergence of a variety of intense peaks visible in the left part of the black spectrum. These peaks can be attributed to Raman-active modes of various copper oxides formed at the graphene/copper interface [16, 20], where the three most prominent peaks are due to cupric oxide CuO (500 cm^{-1}), cuprous oxide Cu_2O (640 cm^{-1}) and copper hydroxide $Cu(OH)_2$ (800 cm^{-1}) and the less prominent peaks (422 cm^{-1}, 1284 cm^{-1}) are overtones of the Cu_2O mode. All these peaks are absent in the red spectrum, which has been taken at a spot where the Cu surface is not yet oxidized.

As the oxidation process proceeds with time and the oxide layer underneath the graphene grows in thickness, the intensity of these peaks relative to the graphene modes rises. The oxidation process in water saturated air essentially works by the functionalization of the graphene edge by water molecules forming oxygen containing groups like hydroxyl, which in recombination allow the formation of Cu_2O [16]. This mechanism allows an advanced quantification of the oxidation status of the graphene/copper interface in addition to microscope imaging as the relative intensity of the Cu_2O peaks rise with ongoing oxidation. As illustrated in figure 1(b), the graphene crystal can only be delaminated from the copper oxide by means of a dry-transfer technique using a soft stamp based on hBN [6] or other 2D materials [10].

In this work, the graphene was delaminated from the oxidized Cu foil using an exfoliated hexagonal boron nitride (hBN) crystal placed on top of a polymethyl-methacrylate (PMMA) and polyvinyl-alcohol (PVA) stamp that itself is fixed on a small block of polydimethylsiloxane (PDMS). Subsequently, the graphene/hBN stack was placed on a second hBN crystal that was previously exfoliated onto a Si^{++}/SiO_2 substrate. The PDMS block was peeled off and the PVA and PMMA layers were dissolved in hot water (95 °C) and acetone, respectively. Figure 1(d) shows an optical image of one of the final hBN/CVD-Gr/hBN heterostructures.

Again we used confocal Raman spectroscopy to characterize the structural quality of the heterostructures. In figure 1(c) we show representative Raman spectra of the sandwich shown in figure 1(d) recorded with $\lambda = 457$ nm (blue spectrum) and, for comparison, at the same location, with $\lambda = 532$ nm (green spectrum). The spectra exhibit the characteristic Raman hBN peak at $\omega_{\mathrm{hBN}} = 1366\ \mathrm{cm}^{-1}$ as well as the Raman G and 2D peaks of graphene [18, 19, 21, 22]. The low frequency copper-oxide peaks have disappeared entirely and the D-peak remains absent within the entire heterostructure (note that the appearing Si-peaks are all well understood [23]). This highlights the contamination-free and non-invasive nature of our dry-transfer process. A difference of around 20 cm^{-1} in the 2D peak position ω_{2D} recorded with the blue and green laser, respectively, can be explained by the energy-dispersive nature of the 2D peak [24].

Since the overall Raman intensity yield from the green laser excitation is much higher than the intensity obtained from the blue laser and to allow a comparison with previous works, we discuss further examinations with the green laser only. The 2D-peak exhibits a narrow full-width-at-half-maximum (FWHM) of 17 cm^{-1}. This value is comparable to other reported high mobility samples obtained from both exfoliated and CVD-grown graphene [6, 7, 25]. The positions of the Raman G and 2D peaks around $\omega_G = 1582\ \mathrm{cm}^{-1}$ and $\omega_{2D} = 2680\ \mathrm{cm}^{-1}$ point to an overall low doping concentration of the graphene [26]. Figure 1(e) shows a spatial map of the line width of the 2D peak, Γ_{2D}, of the hBN/CVD-Gr/hBN heterostructures shown in figure 1(d). Γ_{2D} is lowest at regions where the graphene is fully encapsulated in hBN with values around 17 cm^{-1} indicating very small nanometer-scale strain variations over the entire graphene layer [27, 28].

Areas with the lowest mean Raman 2D line width values are considered for devices. Electron beam lithography as well as SF_6-based reactive ion etching (RIE) were employed to fabricate Hall-bar-shaped structures with a channel of 2.3 μm in width and 4 μm in length. The Hall-bar structures were then covered by an additional hBN crystal to protect the devices from additional contaminations and quality degradation over time. A second RIE step and metal evaporation were performed to create one dimensional Cr/Au (5 nm/95 nm) contacts. An optical image of the final device is shown in figure 1(f). For electrostatic gating, we use the highly p-doped silicon at the back side of the substrate that is covered by a 300 nm thick silicon oxide layer, where the contacted sandwich structure is resting on. Taking the thickness of the bottom hBN crystal into account this leads to a back gate (BG) capacitance per area A of $C_{\mathrm{BG}}/A = \varepsilon_0\varepsilon_r/e(d_{\mathrm{Si}} + d_{\mathrm{hBN}}) \approx 6.4 \times 10^{10}\ \mathrm{cm}^{-2}\mathrm{V}^{-1}$, where ε_0 is the dielectric constant, $\varepsilon_r \approx 4$ is the relative permittivity of hBN and SiO_2, e is the electron charge and $d_{\mathrm{Si}} = 300$ nm and $d_{\mathrm{hBN}} = 45$ nm are the thicknesses of the hBN crystal and the SiO_2 layer, respectively.

Transport measurements were performed in a pumped ^{4}He cryostat system with a base temperature of 1.8 K (B-fields up to 9 T) and in a ^{3}He cryostat system with a base temperature of 300 mK (B-fields up to 35 T). We used standard lock-in techniques to measure the four-terminal resistance as well as the Hall voltage for extracting the Hall conductivity. When cooled down to 4.2 K the device showed a low overall doping ($n = 5 \times 10^9\ \mathrm{cm}^{-2}$, with the charge-neutrality point (CNP) situated close to zero gate voltage, $V_{\mathrm{CNP}} = -0.8$ V) and low residual charge

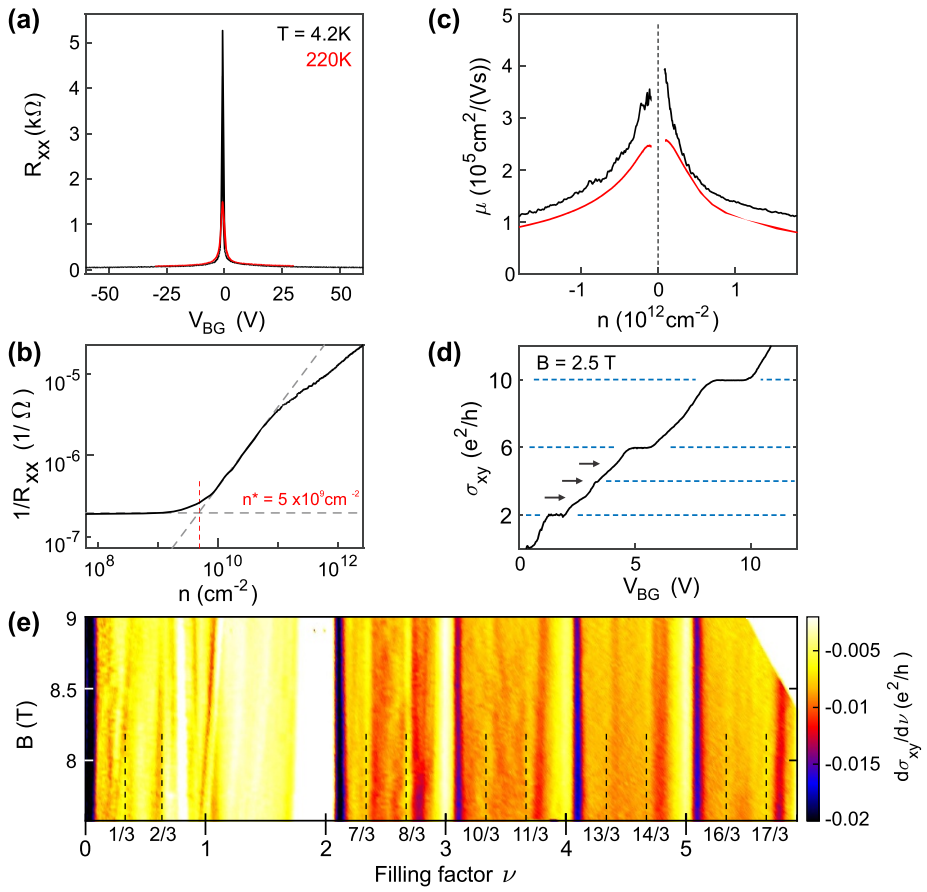

Figure 2. Low temperature magneto-transport measurements (a) Four terminal resistance R_{xx} as function of back gate voltage V_{BG} at a temperature of 220 K (red) and 4.2 K (black). (b) The inverse four terminal resistance $1/R_{xx}$ as function of the charge carrier density n. The intercept of two lines following the regimes of constant slope provides an estimate of the residual charge carrier fluctuations $n^* = 5 \times 10^9$ cm^{-2}. (c) Carrier mobility μ as function of charge carrier density n for $|n| > 5 \times 10^{10}$ cm^{-2}. (d) Hall conductivity σ_{xy} as function of back gate voltage V_{BG} at a perpendicular magnetic field of $B = 2.5$ T ($T = 1.8$ K). The black arrows highlight the integer conductance plateaus due to the lifting of the fourfold Landau level degeneracy. (e) Landau fan diagram. Differential Hall conductivity $d\sigma_{xy}/d\nu$ as function of filling factor ν and magnetic field B recorded at $T = 1.8$ K.

carrier inhomogeneities of $n^* = 5 \times 10^9$ cm^{-2}, see figures 2(a) and (b). These findings are in good agreement with spatially-resolved confocal Raman measurements on the heterostructure as well as with earlier works on dry-transferred CVD graphene [6, 7].

Figure 2(c) shows the charge carrier mobility μ as function of charge carrier density n for two different temperatures extracted using the Drude formula $\sigma = ne\mu$, where σ is the electrical conductivity. Close to the CNP, the mobility at 4.2 K increases to values around 350 000 cm^2 (Vs)$^{-1}$ and around 250 000 cm^2 (Vs)$^{-1}$ at 220 K. In agreement with earlier work [12], we observe a slight discrepancy in quality for the two carrier types and will therefore only focus on the electron governed regime for the remainder of this work.

After demonstrating the high electronic quality of the device, we next discuss magnetotransport measurements with the magnetic field applied perpendicular to the graphene layer. Figure 2(d) shows the Hall conductivity σ_{xy} as function of back gate voltage V_{BG} at a fixed magnetic field of 2.5 T. Even at this low magnetic field, the onset of degeneracy lifting into integer quantum Hall states is well visible. This lifting becomes clearer at higher magnetic fields as shown by the Landau fan diagram in figure 2(e), which shows a false-color plot of the differential Hall conductivity $d\sigma_{xy}/d\nu$ as function of the filling factor ν and the magnetic field B. The former is given by $\nu = (V_{BG} - V_{CNP})\alpha h/(eB)$ with V_{BG} being the back gate voltage and h the Planck constant. The lever arm of the back gate $\alpha = 6.34 \times 10^{10}$ cm^{-2}V^{-1} was extracted from quantum Hall measurements and is in good agreement with the value obtained from the parallel plate capacitor model (C_{BG}/A; see above). The Hall conductivity displays well-developed integer quantum Hall plateaus and furthermore reveals clear indications of states at fractional filling factors $p/3$ even below 8 T, as highlighted by the dashed lines.

Fractional quantum Hall (FQH) states can be attributed with a composite fermion filling factor ν^* that can be related to the integer quantum Hall filling factor ν by $\nu = \nu^*/(2p\nu^* \pm 1)$ for CF electrons and $\nu = 1 - \nu^*/(2p\nu^* \pm 1)$ for CF holes, where $2p$ is the vorticity or number of flux quanta attached to one composite fermion. In order to study these fractional

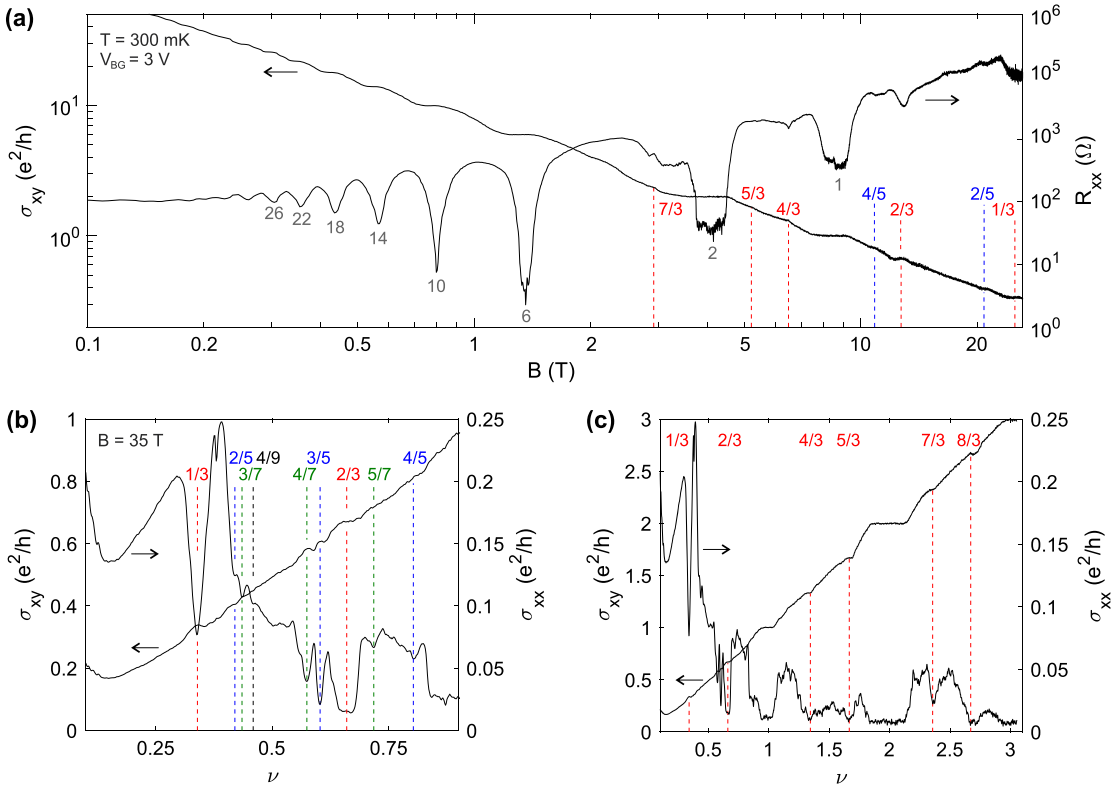

Figure 3. High magnetic field measurements (a) Hall conductivity σ_{xy} and resistance R_{xx} as function of magnetic field B. (b),(c) Hall conductivity σ_{xy} and longitudinal conductivity σ_{xx} as function of filling factor ν at a fixed magnetic field of $B = 35$ T. States with filling factors being integer multiples of $\frac{1}{3}$,$\frac{1}{5}$ and $\frac{1}{7}$ are highlighted in red, blue and green for better visibility.

states in more detail, the device was further characterized at magnetic fields up to 35 T. It should be mentioned at this point that the sample changed slightly after the first cool-down around the CNP. In particular, in contrast to figure 2(e), the 1st Landau level now also becomes clearly visible (see below). Figure 3(a) shows the four terminal resistance R_{xx} as well as the Hall conductivity σ_{xy} as a function of B (logarithmic scale) at a fixed back gate voltage of $V_{\mathrm{BG}} = 3$ V and a temperature of 300 mK. First signatures of the 7/3 state already appear below 3 T and more clearly pronounced FQH states start to develop at higher magnetic fields.

Figures 3(b) and (c) show the Hall conductivity σ_{xy} and the corresponding longitudinal conductivity σ_{xx} as a function of filling factor ν at $B = 35$ T. Well developed plateaus at all $\nu = p/3$ fractional filling factors are visible. Moreover, we can identify all 2-flux CF states ($2p = 2$) up to $\nu^* = 4$ ordered symmetrically around half filling in σ_{xy} as well as in σ_{xx}. Even more, we denote plateaus at $\nu = 5/7$ and 4/5 which can be identified as 4-flux CF hole states ($2p = 4$) with $\nu^* = 1, 2$ centered around $\nu = 3/4$. We emphasize that it is certainly interesting to investigate the 4-flux CF states [5, 29] in more detail and to compare them to other semiconductor FQH systems [30–35]. Indeed, the perspective to grow macroscopic graphene samples using CVD does open this avenue.

These results indicate an outstanding material quality considering the fact that a rather simple Si^{++}/SiO_2 gate oxide was used instead of the state-of-the-art graphitic gating approaches, which allow for precise tuning of the sample edge [36–39] or omit the edge completely when using Corbino geometries or electrostatically defined channels [40–42].

In order to further quantify the robustness of the observed FQH states, we performed temperature dependent activation gap measurements for the most pronounced fractional filling factors $\nu = 2/3$ and $\nu = 4/3$. A set of back-gate traces was recorded at constant magnetic fields for a range of temperature steps. An Arrhenius-like temperature activated model is used to fit the data where the minimum of R_{xx} at a given filling factor ν is assumed to follow $R^{\nu}_{xx,\mathrm{min}} = R\exp(-\Delta_\nu/2k_BT) + R_0$, where k_B is the Boltzmann constant, Δ_ν is the activation gap and R_0 is a resistance offset. Figure 4(a) shows a fit of the R_{xx} minimum minus the offset R_0 at 4/3 filling as a function of temperature between 300 mK and 20 K at $B = 30$ T; the corresponding resistance traces are shown in the inset. The extracted results for $\Delta_{2/3}/k_B$ and $\Delta_{4/3}/k_B$ as function of the magnetic field are shown in figure 4(b). The activation gaps increase roughly linearly with magnetic field reaching a value of 29 K and 24 K, respectively, at $B = 35$ T. This behaviour is in good quantitative agreement with other studies on FQH states in graphene, where values in

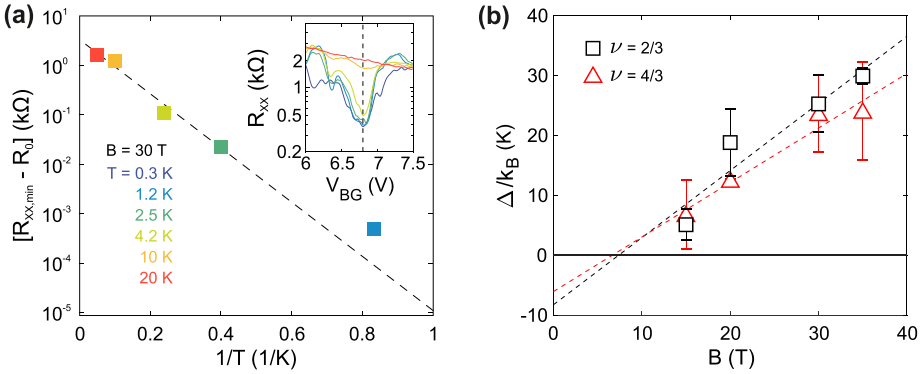

Figure 4. Activation gap measurements (a) Bulk resistance $R_{xx,\mathrm{min}}$ of the 4/3 state corrected by an offset $R_0 = 390\ \Omega$ (see text) as function of inverse temperature $1/T$ at a constant magnetic field of 30 T. The dashed line shows a fit of the temperature activated model $R_{xx,\mathrm{min}} - R_0 = R\exp(-\Delta_\nu/2k_BT)$. The inset illustrates the vanishing bulk resistance dips when increasing T from 300 mK to 20 K. (b) Extracted activation gaps Δ as function of magnetic field for the 2/3 and 4/3 fractional quantum Hall states. Dashed lines represent linear fits.

the range of 30 to 60 K were reported for $\Delta_{2/3}/k_B$ [12, 41] and 16 K for $\Delta_{4/3}/k_B$ [3]. Assuming the B-field dependence being purely given by the CF Zeeman energy (reduced by Landau level broadening) following $\Delta_\nu = \frac{1}{2}\mu_B g B + \Gamma_\nu$, where μ_B is the Bohr magneton and g is the Landé g factor, we can interpret the intercepts Γ_ν as a measure of the disorder-induced Landau-level broadening. In our device we extract Γ values between 6 and 8 K, which is in agreement with values of around 10 K on mechanically exfoliated graphene reported in other studies [3, 12, 41]. The extracted values of the g factor, ranging between 2.7 and 3.4 are roughly a factor 2 smaller compared to values reported in references [12, 41]. Since the g factor is known to strongly depend on the electron-electron interaction renormalization [43] this value may crucially depend on the electrostatic environment substantially influenced by the different gating technologies.

In summary, we have demonstrated the presence of fractional quantum Hall states in CVD-grown graphene underlining the high electronic quality of this material when assembled into heterostructures by a dry-transfer process. Neither CVD growth on Cu substrates nor the oxidation of the Cu surface via water intercalation nor the dry-transfer process induce enough disorder to quench the interaction-driven formation of composite fermions. Even though using a conventional silicon gate to tune the carrier density, CF states emerge even at moderate magnetic fields below 3 T. The full spectrum of 2-flux states up to $\nu^* = 4$ could be identified at $B = 35$ T as well as several 4-flux states. The results are unambiguously proving that the high quality of CVD-grown graphene equals that of mechanically exfoliated graphene flakes. Therefore, a new generation of large-area ultra high quality devices might be achieved using scalably grown 2D materials to dry-transfer CVD graphene and open the door to a deeper understanding of the interaction effects driving the emergence of CF states in graphene.

Note. During preparation of this manuscript, we became aware of a very recent preprint showing indications of the $-1/3$ state in transferred CVD graphene [44].

Acknowledgment

This project has received funding from the European Union's Horizon 2020 research and innovation programme under grant agreement No. 881603 (Graphene Flagship) and from the European Research Council (ERC) under grant agreement No. 820254, the Deutsche Forschungsgemeinschaft (DFG, German Research Foundation) under Germany's Excellence Strategy - Cluster of Excellence Matter and Light for Quantum Computing (ML4Q) EXC 2004/1 - 390534769, through DFG (BE 2441/9-1 and STA 1146/11-1), and by the Helmholtz Nano Facility [45] at the Forschungszentrum Jülich. K W and T T acknowledge support from the Elemental Strategy Initiative conducted by the MEXT, Japan, Grant Number JPMXP0112101001, JSPS KAKENHI Grant Number JP20H00354 and the CREST(JPMJCR15F3), JST. Part of this work was supported by HFML-RU/NWO-I, member of the European Magnetic Field Laboratory (EMFL).

ORCID iDs

M Schmitz https://orcid.org/0000-0002-3402-3724
K Rubi https://orcid.org/0000-0003-1496-8218

K Watanabe https://orcid.org/0000-0003-3701-8119
B Beschoten https://orcid.org/0000-0003-2359-2718
C Stampfer https://orcid.org/0000-0002-4958-7362

References

[1] Bolotin K I, Ghahari F, Shulman M D, Stormer H L and Kim P 2009 Observation of the fractional quantum Hall effect in graphene *Nature* **462** 196–9
[2] Du X, Skachko I, Duerr F, Luican A and Andrei E Y 2009 Fractional quantum Hall effect and insulating phase of Dirac electrons in graphene *Nature* **462** 192–5
[3] Dean C R *et al* 2011 Multicomponent fractional quantum Hall effect in graphene *Nat. Phys.* **7** 693–6
[4] Feldman B E, Krauss B, Smet J H and Yacoby A 2012 Unconventional sequence of fractional quantum Hall states in suspended graphene *Science* **337** 1196–9
[5] Feldman B E, Levin A J, Krauss B, Abanin D A, Halperin B I, Smet J H and Yacoby A 2013 Fractional quantum Hall phase transitions and four-flux states in graphene *Phys. Rev. Lett.* **111** 076802
[6] Banszerus L *et al* 2015 Ultrahigh-mobility graphene devices from chemical vapor deposition on reusable copper *Sci. Adv.* **1** e1500222
[7] Banszerus L, Schmitz M, Engels S, Goldsche M, Watanabe K, Taniguchi T, Beschoten B and Stampfer C 2016 Ballistic transport exceeding 28 μm in CVD grown graphene *Nano Lett.* **16** 1387–91
[8] Schmitz M, Engels S, Banszerus L, Watanabe K, Taniguchi T, Stampfer C and Beschoten B 2017 High mobility dry-transferred CVD bilayer graphene *Appl. Phys. Lett.* **110** 263110
[9] Banszerus L *et al* 2019 Extraordinary high room-temperature carrier mobility in graphene-WSe_2 heterostructures arXiv: 1909.05358
[10] Banszerus L, Watanabe K, Taniguchi T, Beschoten B and Stampfer C 2017 Dry transfer of CVD graphene using MoS_2-based stamps *Phys. Status Solidi* **11** 1700136
[11] Petrone N, Dean C R, Meric I, van der Zande A M, Huang P Y, Wang L, Muller D, Shepard K L and Hone J 2012 Chemical vapor deposition-derived graphene with electrical performance of exfoliated graphene *Nano Lett.* **12** 2751–6
[12] Ribeiro-Palau R, Chen S, Zeng Y, Watanabe K, Taniguchi T, Hone J and Dean C R 2019 High-quality electrostatically defined Hall bars in monolayer graphene *Nano Lett.* **19** 2583–7
[13] Li X *et al* 2009 Large-area synthesis of high-quality and uniform graphene films on copper foils *Science* **324** 1312–14
[14] Chen S *et al* 2013 Millimeter-size single-crystal graphene by suppressing evaporative loss of Cu during low pressure chemical vapor deposition *Adv. Mater.* **25** 2062–5
[15] Hao Y *et al* 2013 The role of surface oxygen in the growth of large single-crystal graphene on copper *Science* **342** 720–3
[16] Luo D *et al* 2017 Role of graphene in water-assisted oxidation of copper in relation to dry transfer of graphene *Chem. Mater.* **29** 4546–56
[17] Choi J, Koo S, Song M, Jung D Y, Choi S-Y and Ryu S 2020 Varying electronic coupling at graphene–copper interfaces probed with Raman spectroscopy *2D Mater.* **7** 025006
[18] Ferrari A C *et al* 2006 Raman spectrum of graphene and graphene layers *Phys. Rev. Lett.* **97** 187401
[19] Ferrari A C and Basko D M 2013 Raman spectroscopy as a versatile tool for studying the properties of graphene *Nat. Nanotechnol.* **8** 235–46
[20] Galbiati M, Stoot A C, Mackenzie D M A, Bøggild P and Camilli L 2017 Real-time oxide evolution of copper protected by graphene and boron nitride barriers *Sci. Rep.* **7** 39770
[21] Graf D, Molitor F, Ensslin K, Stampfer C, Jungen A, Hierold C and Wirtz L 2007 Spatially resolved Raman spectroscopy of single- and few-layer graphene *Nano Lett.* **7** 238–42
[22] Forster F, Molina-Sanchez A, Engels S, Epping A, Watanabe K, Taniguchi T, Wirtz L and Stampfer C 2013 Dielectric screening of the Kohn anomaly of graphene on hexagonal boron nitride *Phys. Rev.* B **88** 085419
[23] Kallel T, Dammak M, Wang J and Jadwisienczak W M 2014 Raman characterization and stress analysis of AlN:Er3+ epilayers grown on sapphire and silicon substrates *Mater. Sci. Eng.* B **187** 46–52
[24] Berciaud S, Li X, Htoon H, Brus L E, Doorn S K and Heinz T F 2013 Intrinsic line shape of the Raman 2D-mode in freestanding graphene monolayers *Nano Lett.* **13** 3517–23
[25] Wang L *et al* 2013 One-dimensional electrical contact to a two-dimensional material *Science* **342** 614–17
[26] Lee J E, Ahn G, Shim J, Lee Y S and Ryu S 2012 Optical separation of mechanical strain from charge doping in graphene *Nat. Commun.* **3** 1024
[27] Couto N J G, Costanzo D, Engels S, Ki D-K, Watanabe K, Taniguchi T, Stampfer C, Guinea F and Morpurgo A F 2014 Random strain fluctuations as dominant disorder source for high-quality on-substrate graphene devices *Phys. Rev.* X **4** 041019
[28] Neumann C *et al* 2015 Raman spectroscopy as probe of nanometre-scale strain variations in graphene *Nat. Commun.* **6** 8429
[29] Goldman H and Fradkin E 2018 Dirac composite fermions and emergent reflection symmetry about even-denominator filling fractions *Phys. Rev.* B **98** 165137
[30] Du R R, Stormer H L, Tsui D C, Yeh A S, Pfeiffer L N and West K W 1994 Drastic enhancement of composite fermion mass near Landau level filling $\nu = \frac{1}{2}$ *Phys. Rev. Lett.* **73** 3274–7
[31] Yeh A S, Stormer H L, Tsui D C, Pfeiffer L N, Baldwin K W and West K W 1999 Effective mass and g factor of four-flux-quanta composite fermions *Phys. Rev. Lett.* **82** 592–5
[32] Pan W, Stormer H L, Tsui D C, Pfeiffer L N, Baldwin K W and West K W 2000 Effective mass of the four-flux composite fermion at $\nu = 1/4$ *Phys. Rev.* B **61** R5101–R5104(R)
[33] Onoda M, Mizusaki T and Aoki H 2001 Effective-mass staircase and the Fermi-liquid parameters for the fractional quantum Hall composite fermions *Phys. Rev.* B **64** 235315
[34] Pan W *et al* 2008 Experimental studies of the fractional quantum Hall effect in the first excited Landau level *Phys. Rev.* B **77** 075307
[35] Hossain M S, Ma M K, Mueed M A, Kamburov D, Pfeiffer L N, West K W, Baldwin K W, Winkler R and Shayegan M 2019 Geometric resonance of four-flux composite fermions *Phys. Rev.* B **100** 041112
[36] Overweg H *et al* 2018 Electrostatically induced quantum point contacts in bilayer graphene *Nano Lett.* **18** 553–9
[37] Banszerus L, Frohn B, Epping A, Neumaier D, Watanabe K, Taniguchi T and Stampfer C 2018 Gate-defined electron–hole double dots in bilayer graphene *Nano Lett.* **18** 4785–90
[38] Zibrov A A, Spanton E M, Zhou H, Kometter C, Taniguchi T, Watanabe K and Young A F 2018 Even-denominator fractional quantum Hall states at an isospin transition in monolayer graphene *Nat. Phys.* **14** 930–5
[39] Kim Y, Balram A C, Taniguchi T, Watanabe K, Jain J K and Smet J H 2018 Even denominator fractional quantum Hall

states in higher Landau levels of graphene *Nat. Phys.* **15** 154–8
[40] Yan J and Fuhrer M S 2010 Charge transport in dual gated bilayer graphene with corbino geometry *Nano Lett.* **10** 4521–5
[41] Zeng Y, Li J I A, Dietrich S A, Ghosh O M, Watanabe K, Taniguchi T, Hone J and Dean C R 2019 High-quality magnetotransport in graphene using the edge-free corbino geometry *Phys. Rev. Lett.* **122** 137701
[42] Chen S, Ribeiro-Palau R, Yang K, Watanabe K, Taniguchi T, Hone J, Goerbig M O and Dean C R 2019 Competing fractional quantum Hall and electron solid phases in graphene *Phys. Rev. Lett.* **122** 026802
[43] Schulze-Wischeler F, Mariani E, Hohls F and Haug R J 2004 Direct measurement of the *g* factor of composite fermions *Phys. Rev. Lett.* **92** 156401
[44] Pezzini S, Mišeikis V, Pace S, Rossella F, Watanabe K, Taniguchi T and Coletti C 2020 Ideal electrical transport using technology-ready graphene 2D Mater. **7** 041003
[45] Albrecht W, Moers J and Hermanns B 2017 HNF - Helmholtz nano facility *J. Large-Scale Res. Facil. JLSRF* **3** 112